Getting Physical with Your Chemistry: Mechanically Investigating Local Structure and Properties of Surfaces with the Atomic Force Microscope

William F. Heinz
Department of Physiology, Johns Hopkins School of Medicine, Baltimore, MD 21205

Jan H. Hoh*
Department Chemical Engineering, Johns Hopkins University, Baltimore, MD 21218; Department of Physiology,
Johns Hopkins School of Medicine, Baltimore, MD 21205; *jhoh@jhmi.edu*

The atomic force microscope (AFM) *(1)* has emerged as a powerful tool for investigating nanoscale structures, dynamics, and forces at interfaces. AFM has matured dramatically in the almost 20-year history of the instrument. As an imaging tool, the strength of the instrument lies in its exceptionally high contrast and fairly high resolution, combined with its ability to function in environments from ultrahigh vacuum to liquid solutions. Because the single-atom and single-molecule contrast originates from picoNewton intermolecular forces, the AFM can investigate mechanically the chemical properties of individual molecules, surfaces, and materials using suitably designed probes. The nanometer dimensions of the AFM tip and the precision positioning system facilitate modification and manipulation of the sample. AFMs are now sufficiently robust and accessible that they have found their way into undergraduate science curricula *(2–5)*. This article will discuss the current state of the art of AFM in terms of imaging, force measurement, and sample manipulation and its application to physical chemistry. We use primarily biological systems as examples for how the AFM can be used although the principles advanced are based on general physical chemistry.

Instrumentation

Basic Setup

In its simplest conceptual form, an AFM can be thought of as a very small ball on a very weak spring (Figure 1). Information about a sample is obtained by measuring deflections of the spring as the ball interacts with the sample. By translating the ball relative to the sample, surface properties can be spatially resolved. In practice the spring in an AFM is usually a silicon or silicon nitride (Si_3N_4) microfabricated cantilever (typical dimensions: l = 100 μm, w = 20 μm, t = 1 μm) with a probe, usually an integrated tip (radius of curvature $R_c \approx$ 5–50 nm), at the end (Figure 2). The cantilever behaves as a Hookian spring with a resonant frequency, f_0, between 5 and 500 kHz and a spring constant, k, between 0.001 and 100 N/m. Any interaction force on the tip deflects the cantilever a quantity proportional to its spring constant. Tip interactions with the sample are detected by monitoring the reflection of a laser off the cantilever with a split-segment photodiode. This optical lever geometry amplifies the cantilever's end-slope (which in the ideal case corresponds to deflection) and yields a detection limit on the

order of 0.1 Å *(6)*. Thus the AFM is sensitive to intermolecular forces as small as fractions of a picoNewton with no real upper bounds, although, generally, forces in the range 10 pN–10 nN are used.

In an AFM a piezo-controlled system moves the sample relative to the tip in a raster pattern in the *x*–*y* plane for imaging or in a ramp in the *z* direction for force measurements (Figure 1). In most instruments, either the sample is attached to an *x*-, *y*-, and *z*-piezo tube and is moved under a fixed cantilever and tip (sample scanning) or the cantilever is attached to the piezos and is moved above a clamped sample (tip scanning) usually on an inverted optical microscope. However, there are a number different implementations. There is, for example, one commercial instrument that scans the sample using *x* and *y* piezos mounted on an inverted microscope stage and a *z* piezo attached to the cantilever, effectively decoupling the *z* axis from *x*–*y*-piezo motions. The time resolution of cantilever deflection measurements, typically limited by the digitizing circuits, is about 5 μs. For some cantilevers this allows significant over-sampling of the resonance. However, most positioning systems used have feedback-loop bandwidths of < 1 kHz, which limits the scanning speed. Recent advances in cantilever and instrument design have significantly improved collection times *(7, 8)*.
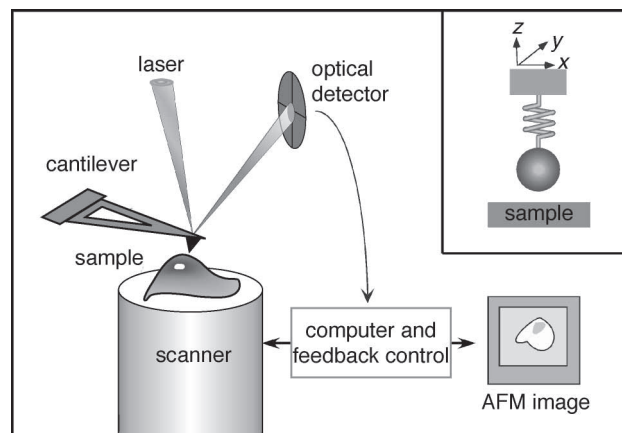

Figure 1. Schematic of a common implementation of the atomic force microscope. Inset: Conceptual representation of the instrument as a small ball on a weak spring interacting with surface.

Cantilevers

Although sophisticated models of cantilever dynamics in different environments and operational modes exist (9), significant insight can be gained if one considers AFM cantilevers as springs that obey simple Newtonian mechanics,

$$F = kd \qquad (1)$$

where F is the force on the spring, k is the spring constant, and d is the deflection of the spring. The spring constant depends on the geometry and material of the cantilever. For a simple beam of length l, width w, and thickness t, and Young's modulus E, the spring constant is

$$k_{\text{beam}} = \frac{Ewt^3}{4l^3} \qquad (2)$$

Most cantilevers are fabricated from silicon ($E \approx 160$ GPa) or Si_3N_4 ($E \approx 300$ GPa) with dimensions: $l \approx 100$ μm, $w \approx 20$ μm, $t \approx 1$ μm. Commercial cantilevers have $k = 0.001$–100 N/m and are either beam or V-shaped (Figures 2A and 2B).
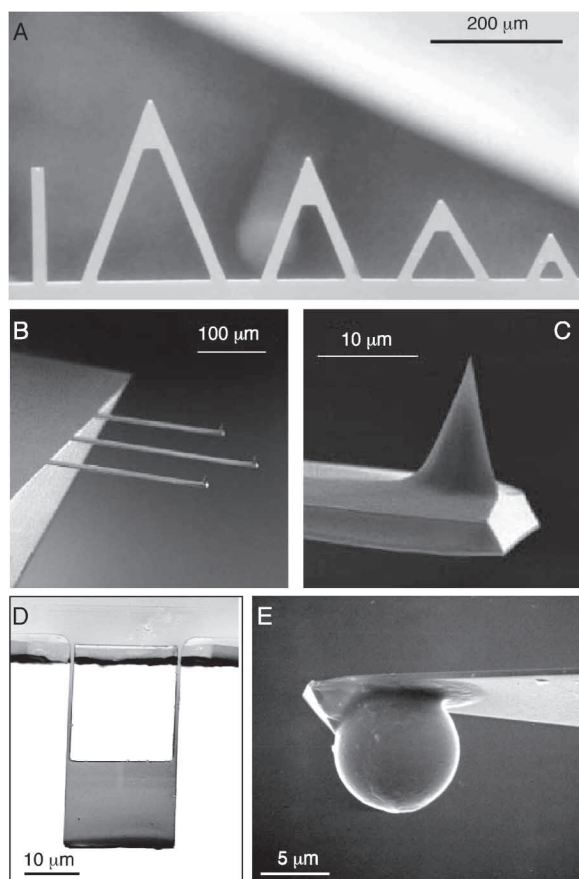
Figure 2. Scanning electron micrographs of some AFM cantilevers and tips: (A) Si_3N_4 cantilevers with beam and V-shaped lever, (B) Si cantilevers with integrated conical tips (Mikromasch, Inc), (C) detail of integrated Si tip, (D) skinny-legged cantilever fabricated by focused-ion-beam milling, and (E) microsphere glued to cantilever (note the pyramidal tip next to the sphere).

The resonant frequency, f_0, of a cantilever depends on k as well as the mass of the lever, m:

$$f_0 = \frac{1}{2\pi}\sqrt{\frac{k}{m}} \qquad (3)$$

Most cantilevers have f_0 between 5 and 500 kHz. In solution the resonant frequency can be significantly lower than in air. It has been shown that

$$\frac{\omega_S}{\omega_V} = \left(1 + \frac{\pi \rho_F w}{4 \rho_C t}\right)^{-1/2} \qquad (4)$$

where ω_S and ω_V are the resonant frequencies in solution and vacuum, respectively, and ρ_F and ρ_C are the fluid and cantilever densities, respectively (10).

Because cantilevers oscillate with thermally-driven motion about an equilibrium deflection, even in the absence of any interaction force (there is always the spring potential), there exists a minimum-detectable force, F_{min}, for cantilevers

$$F_{\text{min}} = \sqrt{4 k_B T C_{\text{damp}} B} \qquad (5)$$

where k_B is Boltzmann's constant, T is the absolute temperature, C_{damp} is the coefficient of viscous damping and is proportional to the surface area of the cantilever, and B is the measurement bandwidth (11). For commercial cantilevers in air F_{min} is 10–20 pN. In solution this increases significantly owing to the increase in C_{damp}.

The combination of f_0 and F_{min} limits the speed and sensitivity of AFM measurements, especially in solution (12). One way to optimize k and increase f_0 is to shorten the cantilever and minimize its thickness. Examination of eqs 2 and 3 shows that k does not change if l is decreased while keeping t/l constant; however, independent of t, f_0 increases with $1/l^2$. Cantilevers with $f_0 > 500$ kHz have been made with spring constants on the order of 0.1 N/m (7, 11). Another approach is to optimize the cantilever leg widths by minimizing the ratio w/t in eq 4. Thin-legged cantilevers made by ion-beam milling commercial levers have higher ω_S and lower C_{damp} than unmodified levers (13) (Figure 2D).

Calibration

Despite the simple Hookian behavior of AFM cantilevers, determining the spring constant of a given lever is not as simple as learning its dimensions. A number of practical considerations make accurate calculations of the spring constant impossible in most situations. For example, the lengths and widths of cantilevers are typically known to within a few percent, but the thickness is not. Photolithographic techniques are used to pattern cantilever shapes, but the thickness is determined by etching or thin-film deposition—less well-controlled processes, even within the same wafer. Because f_0 depends on the third power of t, small differences in t result in large changes in k. Furthermore, cantilevers often have a reflective coating on the top side to maximize reflection of the detection laser, adding to the thickness and modifying the overall E.

There are several experimental methods to calibrate the spring constant of the cantilever. Adding spheres of known mass to the end of the cantilever and measuring the resulting f_0 can lead to a k using a variant of eq 3 in which m is re-

placed with $m^* = m + M$ (M is the added mass) *(14)*. The spring constant can be found also by measuring the cantilever's deflection as it is pushed against a macroscopically calibrated spring *(15)* or a precalibrated AFM cantilever *(16)*. There are several methods to extract k from analysis of thermally induced oscillations of the cantilever *(9, 17, 18)*. Although each vibration mode of the cantilever oscillates with $k_B T$, only the first mode significantly contributes to the measured deflection of a free cantilever, and the spring constant is

$$k = \frac{4 k_B T}{3 \langle d_{OL}^2 \rangle} \qquad (6)$$

where $\langle d_{OL}^2 \rangle$ is the mean square deflection measured using an optical lever.

The above methods all depend on accurate measurements of the cantilever's deflection. The key instrument parameter required to quantify the deflection is the sensitivity of the split-segment photodiode to the cantilever deflection. To determine the sensitivity, the z piezo is moved a known distance such that the tip is pushed onto a hard surface, and the cantilever deflects a quantity equal to the z piezo's motion (Figure 3A). The ratio of the z-piezo motion to the change in voltage from the photodiode while the tip is in contact gives the sensitivity in nm/V. Other methods for finding the sensitivity include the photodiode voltage shift *(19)* and a viscosity-based method *(20)*. The sensitivity measurement depends on a number of factors that contribute to the quality of the optical lever. First, the effective shape and position of the laser spot on the photodiode can vary owing to Poynting instability of the laser itself, not just cantilever deflection (Figure 3B). Single-mode optical fibers that deliver the laser light to the AFM can minimize this. Also, the position of the spot on the back of the cantilever (in directions parallel and perpendicular to the base of the lever) has measurable effect on the sensitivity *(19, 21)*. Finally, the optical lever measures the end-slope of the cantilever, not the deflection *(6, 17)*. The assumption that end-slope is proportional to tip deflection is not always valid; in fact, the tilt of the cantilever relative to the sample increases the effective spring constant by 10–20% *(22)*. The z piezo, upon which all distance measurements are based, can be calibrated using interferometry *(23)*. The end result is that, in general, there is at least a 20% uncertainty in measurements of k, and in the best conditions, a 10% uncertainty.

Tips

AFM tips are designed integrated with the cantilever, and they are fabricated using etches that differentially etch appropriate crystal planes or bonds in the cantilever material itself or a mold used to form the tip. Tip geometries, therefore, are typically asymmetric inverted pyramids or cones. Although the tips are usually the same material as the lever *(24)*, some groups have made silicon nitride cantilevers with integrated silicon tips by etching the tips from silicon wafers and then depositing nitride on the base of the tip to form the lever *(25)*. The sharpness of the tip, critical for *x–y* resolution (discussed below), is described by the tip half-angle, the radius of curvature of the tip and the height of the tip. An oxidation-based process can be used to sharpen tips during the fabrication process *(26)*, and electron-beam deposi-
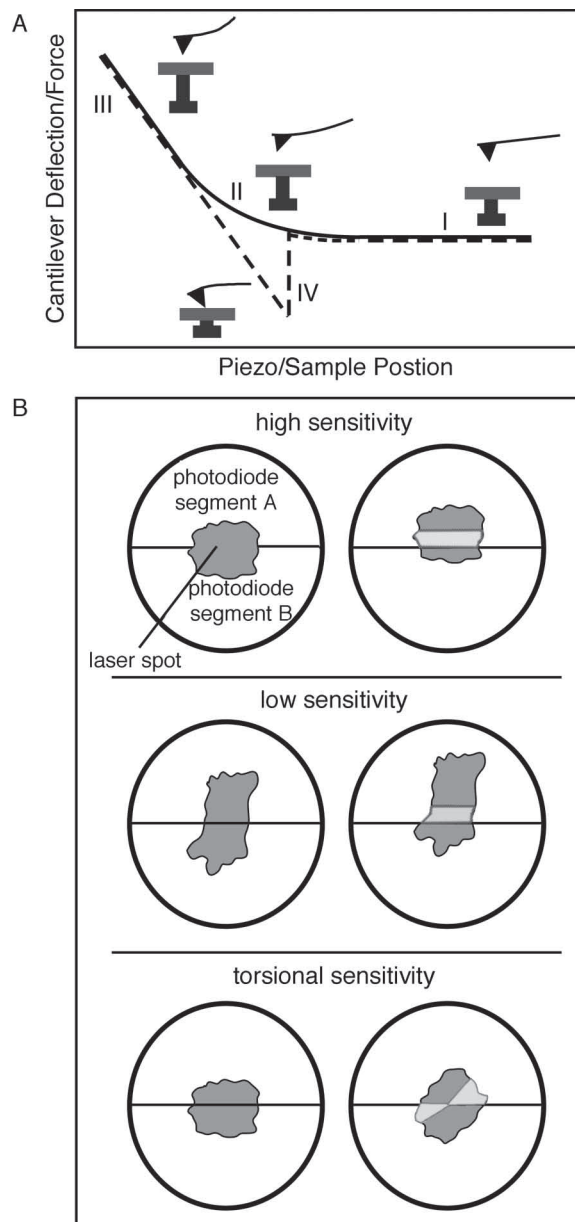
Figure 3. Force curve schematic with photodiode sensitivity illustration: (A) AFM force curve, force as a function of z-piezo position, with approach (solid) and retract (dashed) portions. When the tip is far from the sample, there is zero deflection (I). As the separation distance decreases, long-range repulsive forces deflect the tip away from the sample (II). Once the tip is in contact with a hard sample, the deflection and z-piezo position are linearly coupled (III). Hysteresis in the force curve can result from adhesion between tip and sample (IV). (B) Effect of spot shape and rotation on photodiode sensitivity. For a given deflection, a well-shaped laser spot (top panel) produces a large change in area (light gray) between segments A and B of the photodiode. Because the sensitivity is determined from the (A – B)/(A + B) signal, this corresponds to a high sensitivity. If the spot is misshapen (middle panel), the same deflection results in a smaller relative change in area and a lower sensitivity. Lateral forces on the tip can torque the cantilever and cause the spot to rotate on the photodiode (bottom panel), resulting in anomalous deflection and sensitivity measurements. A quadrant photodiode can quantify the spot rotation.

tion is used to add tall sharp spikes to commercial tips *(27)*. High aspect ratio tips with small R_c (~2 nm) are also produced by focused-ion-beam milling of the etched tip *(28)*.

Tips may be chemically modified as well. Tips are often functionalized directly via physisorption of molecules or via a heterobifunctional linker molecule such as a silane or a poly(ethylene glycol) *(29)*. Probe molecules with exposed thiol groups can be covalently bound to tips sputter coated with gold *(30)*. Secondary structures with well-defined chemistries may be added to tips. For example, surface-functionalized microspheres can be either glued or chemically bonded to tips (Figure 2E), and carbon nanotubes can be attached or grown on tips to provide well-defined structures and chemistries *(31)*.

Imaging

Origin of Contrast

In most imaging modes the AFM has exceptionally high contrast that derives from a combination of the high sensitivity with which the deflection of the cantilever can be measured and the steep distance dependence of the tip–sample interaction. To illustrate, the tip–sample interaction can be represented by the Lennard-Jones potential, $U_{LJ}(r)$, between two identical atoms separated by a distance r,

$$U_{LJ}(r) = \left(\frac{\sigma_R}{r^{12}}\right) - \left(\frac{\sigma_A}{r^6}\right) \qquad (7)$$

where σ_R and σ_A are the LJ constants for the interaction and depend on the atomic species. The force on an atom in a potential is $-dU(r)/dr$ (Figure 4). In the repulsive region of the LJ potential, small changes in r correspond to enormous ($\propto r^{-13}$) changes in force, thus allowing extremely small changes in r to be measured. Depending on the specific sample and experimental conditions, other types of forces will contribute to or dominate the interaction and give rise to different distance dependencies. It should be noted that other forms of microscopy, particularly optical and electron microscopy, typically require contrast-enhancing agents. Other approaches such as NMR and X-ray diffraction exploit large numbers of exceedingly weak interactions to obtain an average description of a sample.

Imaging Modes

The AFM has two basic and common imaging modes, contact and tapping mode (Figure 4D). In each, as the sample scans relative to the tip, the feedback circuit adjusts the position of the z piezo to minimize an error signal at each x–y position. The surface traced out by the z piezo is the so-called height image of the sample.

For contact-mode imaging, the tip is pressed into gentle contact with the sample. The feedback is based on the deflection of the cantilever away from a certain force set-point usually corresponding to an $F(r)$ in the repulsive region of the Lennard-Jones potential. Because the tip is in contact with the sample, the image is usually referred to as a height, or topography, image. This is true only if the surface is hard and does not deform under the load of the tip. In general it is more precise to think of the image as a surface of constant force over the sample. In contact-mode imaging the steep

distance dependence of the interatomic repulsion means that the constant-force surface and van der Waals surface are essentially identical.

In contact mode the process of dragging the tip over a sample may torque the cantilever or deform or damage the sample or the tip. Torsional forces on the cantilever will rotate the detection laser's spot on the photodiode and register an anomalous deflection (Figure 3B). A split-quadrant photodiode can measure this twist, and the resultant signal is the basis for frictional (or lateral) force microscopy. This mode qualitatively distinguishes domains in heterogenous samples (polymer blends or chemically-activated patterned surfaces) by their differential adhesion to the tip. Quantitative friction measurements are difficult to obtain because of large uncertainties in the calibration of the torsional spring constant of the cantilever. Also, topographical features such as edges contribute to the x–y bending of the cantilever, and it is difficult to decouple the topographic contribution from the friction component.
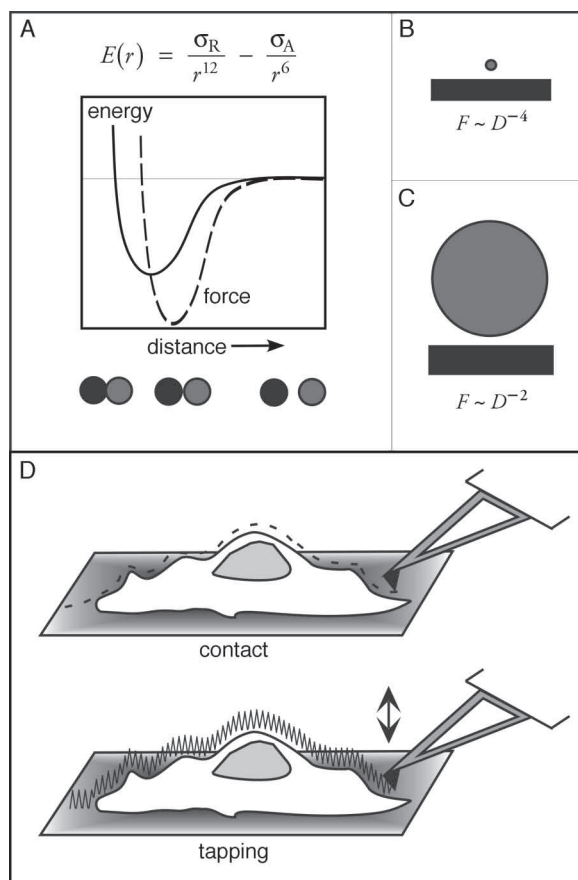

Figure 4. Illustration of the basic contrast mechanism in AFM imaging: (A) The LJ potential and force between two atoms. Note the steep repulsive region for small r. For a tip of radius R separated by a distance D from a planar sample the Derjauguin approximation of the potential predicts (B) a force similar to that between an atom and a plane that scales as D^{-4} for $R \ll D$, or (C) a force like that between a sphere and a plane that scales as D^{-2} for $R > D$. For AFM tips with $R \sim D$, $F(D) \sim D^{-n}$ where $2 < n < 4$. (D) Two common imaging modes of the AFM, contact mode and tapping (or AC) mode.

Oscillating the tip at its resonance frequency during imaging can minimize the destructive effects of lateral interactions of the tip with the sample. Because the amplitude of the oscillating tip is extremely sensitive to its position in the interaction potential, the feedback for this operating mode is based on the change in amplitude of the oscillations as a function of x–y position. This mode, a subset of AC modes (versus DC or time-averaged modes, such as contact) in which a sample is studied via its effect on the cantilever's response to a driving signal *(32)*, is called, variously, tapping mode *(33)*, intermittent-contact mode, MAC mode (for magnetic AC) *(34)*, and others depending on the manufacturer of the instrument and the means by which the cantilever is driven. In other AC modes, such as frequency modulation, the z-piezo is driven and the cantilever response is measured *(35)*.

The contrast in tapping-mode images can originate in the attractive or repulsive part of $U(r)$, depending on the amplitude set-point. When the AFM operates in the attractive part of the potential with a small enough amplitude, height images of the sample can be obtained without the tip contacting the surface (noncontact imaging). If the AFM operates in the repulsive (contact) part of the potential, the forces on the sample are applied normal to the surface, thus minimizing lateral damage. Other signals can be used as the basis for feedback in tapping mode such as the resonance frequency *(36)* and the phase difference between driving signal and the cantilever response *(37)*. The contrast in phase images is interpreted as the energy dissipation by the tip into the sample *(38)*, and it correlates with material and surface properties such as stiffness *(39)* and adhesion *(40)*, but it can include topographic information as well.

Sample Preparation

Samples for AFM need to be immobilized such that they are not displaced by interaction with the cantilever. Large dry samples are frequently immobilized by simply gluing them to a suitable holder. Small dry samples such as powders can be compressed into larger pellets or embedded in a plastic matrix such that their surface is exposed. Large wet samples can present difficulties, and there is no general solution that works for most. In biological AFM, living cells are often grown on glass or plastic supports, and the cells' natural ability to adhere to the surface is exploited. Small wet samples such as proteins and membranes are typically immobilized using some form of adsorption, and the chemistry of the substrate is modified in such a way that the sample binds tightly. Mica, glass, and silica are common substrates that have related surface chemistries based on silicon oxide that can be chemically modified with silanes to enhance attachment and immobilization of a sample. Silanes form a covalent bond with the substrate, and thousands of different functional groups are available as linkers to other molecules of interest or to change the surface properties (e.g., charge, wettability). Samples can be examined in a variety of environments, including vacuum, air, liquids, and temperatures from 1–500 K.

Surface Structure

The high contrast and resolution of the AFM make it particularly effective at imaging macromolecules, including synthetic polymers, adsorbed to surfaces and interfaces, and at relating morphology to surface and material properties *(41)*.

AFM investigations on the morphology of thin films of polymers and polymer blends have shown the effects of preparation conditions including solvent, ratio of polymer species, annealing temperature and time, substrate type, and imaging environment (relative humidity or atmosphere, for example) on surface roughness *(42)*, domain structure *(43)*, defects *(44)*, wettability and dewetting *(45)*, and the thermodynamics of self assembly *(46)*. Similarly, images of supported lipid bilayers (Figure 5A) in solution show the organization of lipid domains and defects in the membranes *(47)*. Membrane proteins and channels have been imaged in physiologic conditions with the AFM, as well *(48)* (Figure 5B). In general, phase images and force measurements are collected on the domains and interfaces in these samples to correlate the morphology with specific material or surface properties.

Single molecules adsorbed to substrates are routinely examined with the AFM (Figure 5C). For example, the effects of surface and solution chemistry on condensation, adsorption, and diffusion of DNA onto surfaces has been extensively studied with the AFM *(49, 50)*.

Dynamics

The AFM can directly measure molecular movements on timescales as fast as milliseconds by recording changes in height or position of single molecules. Fast measurements (ms timescale), such as the observation of lysozyme height fluctuations during catalysis, are performed by positioning the tip over a molecule of interest and monitoring the deflection as a function of time *(51)*. Slower measurements (~100 ms time scale), such as the fluctuations of GroEl protein complex and the interactions of GroEl–GroEs are performed by disabling the slow scan axis during imaging *(52)*. The resulting image is a time sequence of the fluctuations of multiple molecules (Figure 5D). Processes that occur on a timescale
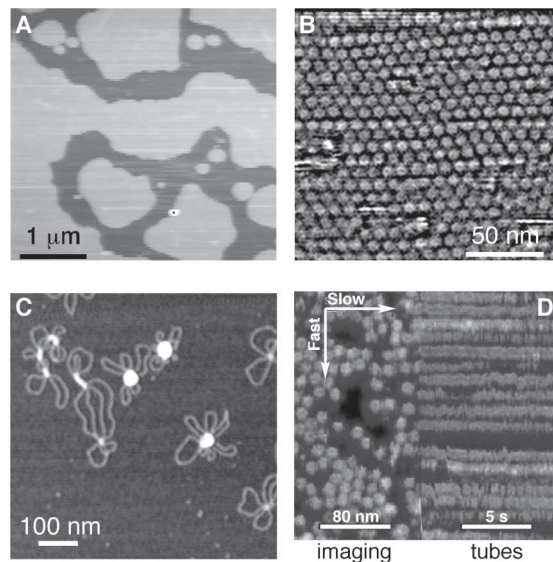

Figure 5. Examples of structures and surfaces that have been imaged by AFM: (A) supported lipid bilayer in solution *(47)*, (B) extracellular surface of the ion channels in a gap-junction membrane in a physiological saline *(48)*, (C) morphology of DNA condensates formed using cationic silanes under ambient (dry) conditions *(50)*, and (D) dynamics of the protein complex GroEL–GroES in solution visualized by disabling the slow scan axis *(52)*.

of minutes and longer, such as the dynamics of crystal growth as a function of salts and protein concentration *(53)*, the evolution of defects in annealing polymer thin films *(44),* and the annealing of polymer crystals *(54)* are monitored by repeatedly scanning the same area.

Image Interpretation

AFM image interpretation is more complicated and fraught with difficulties than might be initially apparent. To illustrate the complexities we discuss some issues with regard to image interpretation, but one should be aware that there are many more factors that can lead to misinterpretation.

AFM image resolution can be divided into z resolution (normal to the surface) and x–y resolution (in the plane of the surface). The instrumental z resolution is determined primarily by the precision with which the cantilever deflection can be measured (~0.1 Å). However, mechanical properties also play a role in z resolution in the image, since interactions of the tip with the sample can cause the sample to move, creating an uncertainty in the z position of the undeformed surface. The x–y resolution of AFM images depends on the dimensions of the tip, z resolution, the dimensions and deformability of the objects being imaged, and the quality (time constant) of the feedback circuit. However, it is important to recall that what can be seen in an image depends on both resolution and contrast. Diffraction-based resolution criteria can be used to overcome weak contrast by effectively averaging over the entire image. Because contrast in AFM images is high at all spatial frequencies, diffraction-based

analyses do not add anything beyond what can be obtained by a direct visual inspection. Thus an appropriate and sufficient resolution measure is the point-to-point resolution, defined essentially as the smallest features that can be resolved in an image. It should be noted that when using feedback to maintain constant force during AFM imaging, the information from the imaging process is spread between the error signal (deflection) image and the height image. In the limit where the feedback loop is off, all the information is in the deflection image. As the feedback loop is turned on and the time constant is gradually decreased, information is increasingly passed to the height image. The data passed are very low frequencies for the long time constants and become higher frequencies for higher time constants. Effectively the feedback loop is a transfer function that produces the height image from the deflection data. Thus the error signal image always contains the highest frequency information, and the frequency content of the height image depends on the feedback loop and scan speed. The resonance frequency of the cantilever and the material properties of the sample place an upper limit on the useful scan speed of the AFM, and the combination of these factors also contribute to the x–y resolution of the image *(12)*. The cantilever and the sample also have finite response times; if the scan speed is too fast, the cantilever will not accurately track the surface of the sample, or the sample may deform under the tip, and the end result will be an image that differs significantly from the true topography of the sample. Taking all these factors into consideration, AFM x–y resolution ranges from 0.1 to 100 nm in general. The highest resolution is obtained on hard flat samples and is usually between 1 and 10 nm for biomolecular imaging.

The apparent dimensions of structures in the height image of a sample can be significantly broadened by the shape of the tip and by contributions from the feedback loop (Figure 6). Because the tip is not an ideal point scanning the surface, the sides of the tip can interact with features on the sample surface before the apex of the tip does, and the feedback will respond to those interactions. Surface features in the resulting images are broadened as a result of the tip contribution. More generally the feature with the smallest radius of curvature, on either the tip or the sample, "images" the other. As a result most AFM images are really a complex mixing of the tip structure with the sample structure *(55)*. Often called a convolution between tip and sample, this mixing is actually a morphological dilation of the sample by the tip (or vice versa) *(56)*. The reverse operation, erosion, requires the image as well as tip shape information. Therefore, there is no way to determine the sample features' true x–y dimensions without knowledge of the tip shape. Standard samples, such as tip arrays and nanoparticles, and reconstruction algorithms can help estimate the tip shape and its contributions to the image *(56)*. Such approaches do not recover information not present in the original image; they only allow tip-bounded areas of the image to be identified. It is important to note that although the tip structure can broaden a sample feature, it does not change distances internal to the structure. For example, a protein dimer with a monomer center-to-center distance of 8 nm might appear to be 35 nm wide owing to tip broadening, but the distance between monomer peaks remains 8 nm.
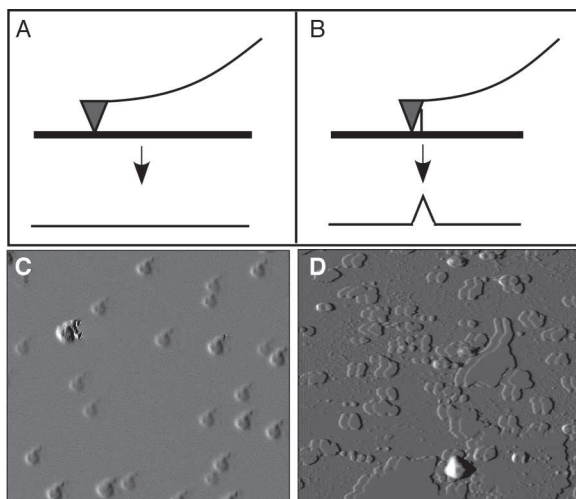

Figure 6. Effect of tip size and shape on image interpretation: (A) In the limiting case of a perfectly flat sample surface (thick line), the height image (thin line) perfectly depicts the sample; (B) On the other hand, if the sample is an infinitely sharp point, then the height image accurately depicts the tip. Actual samples fall between the two limits, and the surface features in the height image contain partial information about the sample and the tip. (C, D) Examples of samples where the tip structure dominates the image. (C) Deflection image of single protein molecules. The constant orientation of the molecules suggests that the morphology is dominated by tip structure contributions to the image and does not reflect molecular structure. (D) Deflection image of supported lipid bilayers on mica in solution. The "shadowing" is due to a double tip.

A particularly vexing problem related to tip broadening is that irregular tip shapes give rise to apparent structure in the image. As we saw above, when the sample is sharper than the tip, the sample is effectively imaging the tip. Thus when the tip is not a well-formed point, has become contaminated during imaging, or for some other reason has unexpected structure, that tip structure appears in the image. This is most easily seen in images of sharply pointed surfaces, where the tip structure is replicated many times in the image (Figure 6C) or where features appear to be duplicated (Figure 6D). True sample features will rotate relative to the scan direction as the sample is rotated, but the common practice of rotating the scan direction does not help in identifying tip contributions to the image. When the scan direction is rotated, the geometry of the tip sample interaction are not changed and both true and tip dominated images will rotate.

Force Spectroscopy

Force Curves

In addition to imaging, the AFM is a powerful tool for the direct interrogation of the local surface chemistry and the material properties of samples. The AFM can probe intermolecular forces over a single point on the sample by recording the cantilever deflection, d, (proportional to the force) as the sample is moved in z. The plot of z against d is called a force curve (Figure 3) and consists of a single approach and retract cycle. To interpret force curves with established theories that describe force as a function of separation distance, D, the force curve must be transformed into a force–distance curve *(57)* (Figure 7A). The distribution of forces and surface characteristics across an area can be investigated by collecting an array of force curves, a force volume, over the area. Distributions of forces at various z positions, isoforce surfaces, and maps of surface and material properties can be extracted from the three-dimensional data set. The AFM is sensitive to a large number of colloidal forces *(58)*. To illustrate, we consider two forces that act on the tip during the approach portion of the force curve (Figures 7A and B). We note that interpreting force curves is even more complex than interpreting AFM images and equally fraught with potential misinterpretation. However, a reasonable treatment of interpretation difficulties and artifacts is beyond the scope of this article, and we will simply warn those interpreting these curves to exercise caution.

van der Waals Forces

The AFM is sensitive to the short-range attractive portion of the Lennard-Jones potential (eq 7) that results from electrostatic interactions between induced dipoles on each atom and is described by the van der Waals force law

$$F_{vdW}(r) = \frac{-\sigma_{vdW}}{r^6} \tag{8}$$

where σ_{vdW} is the strength of the interaction and depends on the species of the atoms, and r is the distance between atoms. In the case of the AFM, instead of a two-atom interaction, we consider the contribution of the extent of the entire tip and sample using the Derjaguin approximation *(59)*. In this case, the total force on a tip a distance D from the sample, $F(D)$, is a summation of all the interatomic interactions in the system,

$$F(D) = \sum F_{ij}(r_{ij}) \tag{9}$$

where $F_{ij}(r_{ij})$ is the force between atoms i and j in the sample and tip, respectively, and r_{ij} is the distance between the atoms. The Derjauguin approximation is applicable to all colloidal forces that may interact with the tip. For the AFM the attractive van der Waals force becomes,

$$F(D) = -\frac{A_H R}{6 D^2} \tag{10}$$

where A_H is the Hamaker constant for the system and R is the tip radius. The D^{-2} dependence results from treating the
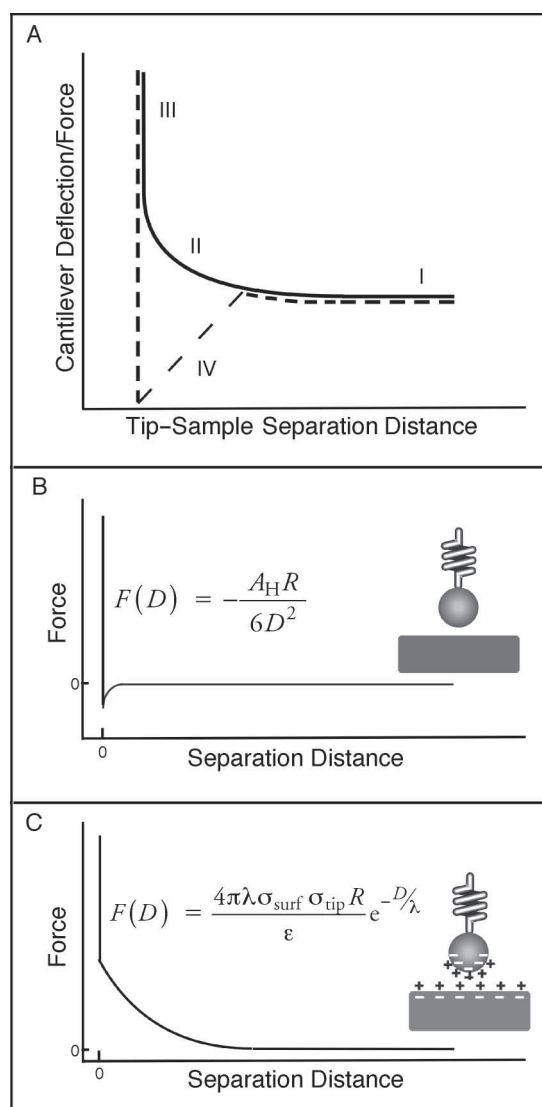

Figure 7. Force–separation curves: (A) force as a function of tip–sample separation distance. The labeled regions in the curve correspond to those in Figure 3A. Examples of force–distance curves of short- and long-range surface forces: (B) van der Waals attraction and jump to contact and (C) electrostatic double-layer repulsion.

tip as a sphere, and other geometries yield D^{-n}, where $2 < n < 4$ (Figure 4B and 4C) *(59)*. AFM measurements of the van der Waals force show a D^{2-4} dependence and Hamaker constants that agree with other methods *(60)*.

During an approach, when the tip is at a position in the attractive potential at which the force gradient is greater than the spring constant of the cantilever, the cantilever will become unstable, and the tip will "jump" to the bottom of the well *(59)*. This jump to contact obscures information about the shape of the attractive potential between the onset of the instability and the bottom of the well.
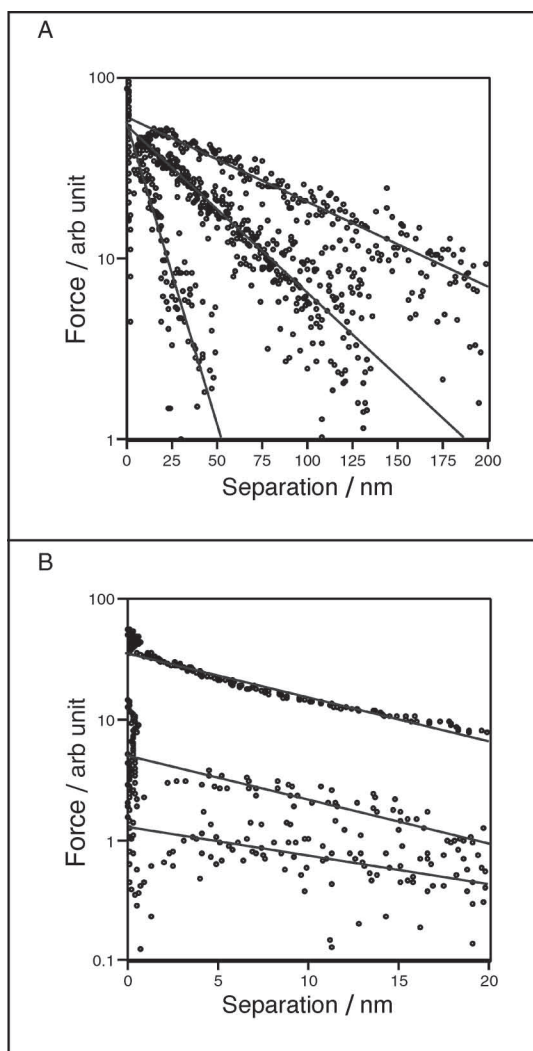

Figure 8. Electrostatic double-layer measurements with the AFM: (A) Effect of salt concentration on Debye length. On a log–linear plot of force versus separation, changing the salt concentration varies the slope of the curve. Steeper slopes correspond to shorter λ. Measurements made on COO⁻ terminated microspheres. (B) Changing the surface charge density of the microspheres (at constant ionic strength) changes the intercept of the curve. Higher σ_{surf} correspond to a larger intercept. The van der Waals attraction and jump-to-contact are evident at small separations.

Electrostatic Double-Layer Force

The AFM can measure surface charge densities and surface potentials by exploiting long-range electrostatic forces in liquid environments. A charged surface in an electrolyte solution creates an ionic gradient that decays with the Debye length, λ, which depends on the ionic strength. The surface charge, σ_{surf}, and the cloud of counterions are called the electrostatic double layer. The interaction between a charged plane and a tip of radius R and surface charge σ_{tip} is modeled using the Debye–Hückel *(59)* formulation,

$$F(D) = \frac{4\pi\lambda\sigma_{surf}\sigma_{tip}R}{\varepsilon} e^{-D/\lambda} \qquad (11)$$

where ε is the dielectric of the medium. Quantitative electrostatic measurements with the AFM are based on the DLVO theory *(59)*, which combines the repulsive forces produced by overlapping electrostatic double layers and the van der Waals attraction (eq 9). At small D, the attractive van der Waals force overpowers the double-layer repulsion, and there is a jump-to-contact event.

To determine the surface charge density of sample surfaces using eq 11, the native surface chemistry of the tip can be exploited (Si_3N_4 has an isoelectric point of 5–6 and is negatively charged at pH 7) or tips can be chemically modified with a particular surface charge density. AFM measurements of surface charge density and Debye length as functions of ionic strength and pH agree with standard DLVO theory (Figure 8), and have been made on samples such as mica, silicon, supported lipid bilayers, membrane proteins, and charged polystyrene spheres *(47, 60, 61)*.

Thermal Noise

One final force measurement technique that deserves mention is the thermal noise approach. Here, the thermally-driven motion of the cantilever can be used to probe the interaction potential of the sample. The cantilever oscillates with k_BT in a potential that is a combination of the harmonic potential of the cantilever ($kd^2/2$) and the interaction potential of the sample, and the potential can be determined using the Boltzman relation *(62, 63)*. Potentials deeper than k_BT can be investigated by driving the cantilever with a white-noise waveform that causes the cantilever to oscillate as if it were at a significantly higher temperature and prevents the cantilever from becoming trapped in the well *(64)*. Thermal-noise techniques are also used to probe the behavior of end-grafted polymers *(65, 66)*.

Conclusion

The AFM has become a extremely versatile instrument for nm- and pN-scale investigations of materials, surfaces, and interfaces. However, despite the remarkable advances in the past 20 years the instrumentation and methods continue to advance at a fast pace. AFM related technology is also expanding into other areas such as sensors, and it is possible that we have not yet seen the most important applications for the technology. The next 20 years promise to be even more exciting than the first 20, as we exploit the capabilities that are now available to understand physical chemistry of surfaces at the nanometer length scale while pushing forward for new ways to look at these problems.

Literature Cited

1. Binnig, G.; Quate, C. F.; Gerber, C. *Phys. Rev. Lett.* **1986,** *56,* 930–933.

2. Aumann, K.; Muyskens, K. J. C.; Sinniah, K. *J. Chem. Educ.* **2003,** *80,* 187–193.

3. Glaunsinger, W. S.; Ramakrishna, B. L.; Garcia, A. A.; Pizziconi, V. *J. Chem. Educ.* **1997,** *74,* 310–311.

4. Lehmpuhl, D. W. *J. Chem. Educ.* **2003,** *80,* 478–479.

5. Zhong, C. J.; Han, L.; Maye, M. M.; Luo, A.; Kariuki, N. N.; Jones, W. E. *J. Chem. Educ.* **2003,** *80,* 194–197.

6. Alexander, S.; Hellemans, L.; Marti, O.; Schneir, J.; Elings, V.; Hansma, P. K.; Longmire, M.; Gurley, J. *J. Appl. Phys.* **1989,** *65,* 164–167.

7. Viani, M. B.; Schaffer, T. E.; Paloczi, G. T.; Pietrasanta, L. I.; Smith, B. L.; Thompson, J. B.; Richter, M.; Rief, M.; Gaub, H. E.; Plaxco, K. W.; Cleland, A. N.; Hansma, H. G.; Hansma, P. K. *Rev. Sci. Instrum.* **1999,** *70,* 4300–4303.

8. Ando, T.; Kodera, N.; Takai, E.; Maruyama, D.; Saito, K.; Toda, A. *Proc. Nat. Acad. Sci. U.S.A.* **2001,** *98,* 12468–12472.

9. Sader, J. E. In *Encyclopedia of Surface and Colloid Science;* Hubbard, A., Ed.; Marcel Dekker, Inc.: New York, 2002; pp 846–856.

10. Chu, W.-H. Technical Report No. 2, DTMB, Contract No. 86396(X), Southwest Research Institute: San Antonio, TX 1963.

11. Viani, M. B.; Schaffer, T. E.; Chand, A.; Rief, M.; Gaub, H. E.; Hansma, P. K. *J. Appl. Phys.* **1999,** *86,* 2258–2262.

12. Butt, H.-J.; Siedle, P.; Seifert, K.; Fendler, K.; Seeger, T.; Bamberg, E.; Weisenhorn, A. L.; Goldie, K.; Engel, A. *J. Microsc.* **1993,** *169,* 75–84.

13. Hodges, A. R.; Bussmann, K. M.; Hoh, J. H. *Rev. Sci. Instrum.* **2001,** *72,* 3880–3883.

14. Cleveland, J. P.; Manne, S.; Bocek, D.; Hansma, P. K. *Rev. Sci. Instr.* **1993,** *64,* 403–405.

15. Jericho, S. K.; Jericho, M. H. *Rev. Sci. Instrum.* **2002,** *73,* 2483–2485.

16. Tortonese, M.; Kirk, M. Micromachining and Imaging, SPIE Proceedings: Bellingham, WA, 1997; Vol. 3009, p 53.

17. Butt, H. J.; Jaschke, M. *Nanotechnolgy* **1995,** *6,* 1–7.

18. Hutter, J.; Bechoefer, J. *Rev. Sci. Instrum.* **1993,** *64,* 1868–1873.

19. Dcosta, N. P.; Hoh, J. H. *Rev. Sci. Instrum.* **1995,** *66,* 5096–5097.

20. Notley, S. M.; Biggs, S.; Craig, V. S. J. *Rev. Sci. Instrum.* **2003,** *74,* 4026–4032.

21. Proksch, R. *Biophys. J.* **2003,** *84,* 471A–471A.

22. Heim, L.-O.; Kappl, M.; Butt, H.-J. *Langmuir* **2004,** *20,* 2760–2764.

23. Jaschke, M.; Butt, H. J. *Rev. Sci. Instr.* **1995,** *66,* 1258–1259.

24. Albrecht, T. R.; Akamine, S.; Carver, T. E.; Quate, C. F. *J. Vac Sci. Technol. A* **1990,** *8,* 3386–3396.

25. Grow, R. J.; Minne, S. C.; Manalis, S. R.; Quate, C. F. *J. Microelectromechanical Systems* **2002,** *11,* 317–321.

26. Boisen, A.; Hansen, O.; Bouwstra, S. *J. Micromech. Microeng.* **1996,** *6,* 58–62.

27. Walters, D. A.; Hampton, D.; Drake, B.; Hansma, H. G.; Hansma, P. K. *Appl. Phys. Lett.* **1994,** *65,* 787–789.

28. Ximan, H. Y.; Russell, P. E. *Ultramicrosc.* **1992,** *42,* 1526–1532.

29. Riener, C. K.; Kienberger, F.; Hahn, C. D.; Buchinger, G. M.; Egwim, I. O. C.; Haselgrubler, T.; Ebner, A.; Romanin, C.; Klampfl, C.; Lackner, B.; Prinz, H.; Blaas, D.; Hinterdorfer, P.; Gruber, H. J. *Analyt. Chim. Acta* **2003,** *497,* 101–114.

30. Noy, A.; Frisbie, C. D.; Rozsnyai, L. F.; Wrighton, M. S.; Lieber, C. M. *J. Am. Chem. Soc.* **1995,** *117,* 7943–7951.

31. Cheung, C. L.; Hafner, J. H.; Lieber, C. M. *Proc. Nat. Acad. Sci. U.S.A.* **2000,** *97,* 3809–3813.

32. Garcia, R.; Perez, R. *Surf. Sci. Rep.* **2002,** *47,* 197–301.

33. Hansma, P. K.; Cleveland, J. P.; Radmacher, M.; Walters, D. A.; Hillner, P. E.; Bezanilla, M.; Fritz, M.; Vie, D.; Hansma, H. G.; Prater, C. B.; Massie, J.; Fukunaga, L.; Gurley, J.; Elings, V. *Appl. Phys. Lett.* **1994,** *64,* 1738–1740.

34. Han, W. H.; Lindsay, S. M.; Jing, T. W. *Appl. Phys. Lett.* **1996,** *69,* 4111–4113.

35. Fritz, M.; Radmacher, M.; Petersen, N.; Gaub, H. E. *J. Vac. Sci. Tech. B* **1994,** *12,* 1526–1529.

36. Roters, A.; Schimmel, M.; Ruhe, J.; Johannsmann, D. *Langmuir* **1998,** *14,* 3999–4004.

37. Tamayo, J.; Garcia, R. *Langmuir* **1996,** *12,* 4430–4435.

38. Cleveland, J. P.; Anczykowski, B.; Schmid, A. E.; Elings, V. B. *Appl. Phys. Lett.* **1998,** *72,* 2613–2615.

39. Raghavan, D.; van Landingham, M.; Gu, X.; Nguyen, T. *Langmuir* **2000,** *16,* 9448–9459.

40. Noy, A.; Sanders, C. H.; Vezenov, D. V.; Wong, S. S.; Lieber, C. M. *Langmuir* **1998,** *14,* 1508–1511.

41. Munz, M.; Cappella, B.; Sturm, H.; Geuss, M.; Schulz, E. *Adv. Polymer Sci.* **2003,** *164,* 87–210.

42. Godovsky, Y. K.; Papkov, V. S.; Magonov, S. N. *Macromol.* **2001,** *34,* 976–990.

43. Miles, M. J.; Jandt, K. D.; McMaster, T. J.; Williamson, R. L. *Coll. Surf. A—Physicochem. Eng. Aspects* **1994,** *87,* 235–243.

44. Hahm, J.; Sibener, S. J. *J. Chem. Phys.* **2001,** *114,* 4730–4740.

45. Gu, X.; Raghavan, D.; Douglas, J. F.; Karim, A. *J. Polymer Sci. B—Polymer Phys.* **2002,** *40,* 2825–2832.

46. Yau, S. T.; Petsev, D. N.; Thomas, B. R.; Vekilov, P. G. *J. Mol. Biol.* **2000,** *303,* 667–678.

47. Heinz, W. F.; Hoh, J. H. *Biophys. J.* **1999,** *76,* 528–538.

48. Hoh, J. H.; Sosinsky, G. E.; Revel, J.-P.; Hansma, P. K. *Biophys. J.* **1993,** *65,* 149–163.

49. Fang, Y.; Spisz, T. S.; Hoh, J. H. *Nucleic Acids Res.* **1999,** *27,* 1943–1949.

50. Fang, Y.; Hoh, J. H. *FEBS Lett.* **1999,** *459,* 173–176.

51. Radmacher, M.; Fritz, M.; Hansma, H. G.; Hansma, P. K. *Science* **1994,** *265,* 1577–1579.

52. Viani, M. B.; Pietrasanta, L. I.; Thompson, J. B.; Chand, A.; Gebeshuber, I. C.; Kindt, J. H.; Richter, M.; Hansma, H. G.; Hansma, P. K. *Nature Struct. Biol.* **2000,** *7,* 644–647.

53. Thompson, J. B.; Paloczi, G. T.; Kindt, J. H.; Michenfelder, M.; Smith, B. L.; Stucky, G.; Morse, D. E.; Hansma, P. K. *Biophys. J.* **2000,** *79,* 3307–3312.

54. Ivanov, D. A.; Amalou, Z.; Magonov, S. N. *Macromol.* **2001,** *34,* 8944–8952.

55. Schwarz U. D.; Haefke, H.; Reimann, P.; Guntherodt, H. *J. Microsc.* **1994,** *173,* 183–197.

56. Villarrubia, J. S. *J. Res. Natl. Instit. Stand. Technol.* **1997,** *102,* 425–454.

57. Butt, H.-J. *Biophys. J.* **1992,** *63,* 578–582.

58. Heinz, W. F.; Hoh, J. H. *Trends Biotechnol.* **1999,** *17,* 143–150.

59. Israelachvili, J. *Intermolecular and Surface Forces: With Applications to Colloidal and Biological Systems,* 2nd ed.; Academic Press: New York, 1992.

60. Butt, H. J. *Biophys. J.* **1991,** *60,* 1438–1444.

61. Larson, I.; Drummond, C. J.; Chan, D. Y. C.; Grieser, F. *Langmuir* **1997,** *13,* 2109–2112.

62. Cleveland, J. P.; Schaffer, T. E.; Hansma, P. K. *Phys. Rev. B* **1995,** *52,* 8692–8695.

63. Heinz, W. F.; Antonik, M. D.; Hoh, J. H. *J. Phys. Chem. B* **2000,** *104,* 622–626.

64. Koralek, D. O.; Heinz, W. F.; Antonik, M. D.; Baik, A.; Hoh, J. H. *Appl. Phys. Lett.* **2000,** *76,* 2952–2954.

65. Gelbert, M.; Roters, A.; Schimmel, M.; Ruhe, J.; Johannsmann, D. *Surf. Interface Anal.* **1999,** *27,* 572–577.

66. Benmouna, F.; Dimitrova, T. D.; Johannsmann, D. *Langmuir* **2003,** *19,* 10247–10253.